Inorganic Chemistry

pubs.acs.org/IC

Article

Synthesis and Magnetic, Optical, and Electrocatalytic Properties of High-Entropy Mixed-Metal Tungsten and Molybdenum Oxides

Rowan R. Katzbaer, William M. Vincent, Zhiqiang Mao,* and Raymond E. Schaak*

Cite This: *Inorg. Chem.* 2023, 62, 7843−7852

Read Online

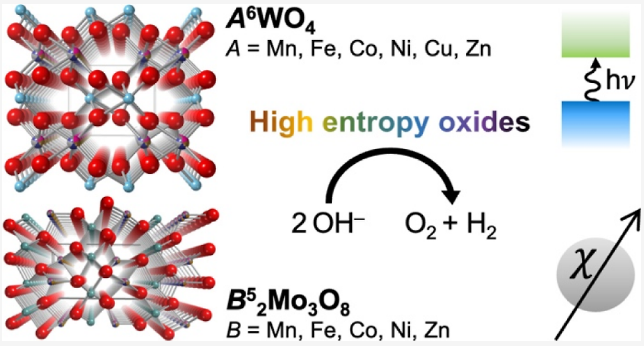

ABSTRACT: High-entropy oxides (HEOs) are of interest for their unique physical and chemical properties. Significant lattice distortions, strain, and tolerance for high-vacancy concentrations set HEOs apart from single-metal or mixed-metal oxides. Herein, we synthesized and characterized the structures and compositions, along with the optical, magnetic, and electrocatalytic properties, of two families of high-entropy mixed-metal tungsten and molybdenum oxides, AWO_4 and $B_2Mo_3O_8$, where A and B are 3d transition metals. The HEOs A^6WO_4 (A = Mn, Fe, Co, Ni, Cu, and Zn) and $B_2{}^5Mo_3O_8$ (B = Mn, Fe, Co, Ni, and Zn), as well as all accessible single-metal AWO_4 and $B_2Mo_3O_8$ parent compounds, were synthesized using high-temperature solid-state methods. X-ray photoelectron spectroscopy analysis of the surfaces revealed that the HEOs largely had the metal oxidation states expected from the bulk chemical formulas, but in some cases they were different than in the parent compounds. A^6WO_4 exhibited antiferromagnetic (AFM) ordering with a Néel temperature of 30 K, which is less than the average of its AFM parent compounds, and had a narrow band gap of 0.24 eV, which is much lower than all of its parent compounds. $B_2{}^5Mo_3O_8$ was paramagnetic, despite the existence of AFM and ferromagnetic ordering in several of its parent compounds and had no observable band gap, which is analogous to its parent compounds. Both A^6WO_4 and $B_2{}^5Mo_3O_8$ exhibited superior catalytic activity relative to the parent compounds for the oxygen evolution reaction, the oxidation half reaction of overall water splitting, under alkaline conditions, based on the overpotential required to reach the benchmark surface area normalized current density. Consistent with literature predictions of OER durability for ternary tungsten and molybdenum oxides, A^6WO_4 and $B_2{}^5Mo_3O_8$ also exhibited stable performance without significant dissolution during 10 h stability experiments at a constant current.

■ INTRODUCTION

High-entropy materials are generally considered to contain five or more elements that randomly mix in nearly equimolar ratios on equivalent atomic sites in a crystal lattice. The five randomly distributed elements represent a theoretical limit to rationalize how their enthalpically unfavorable mixing can occur if the entropy contribution due to configurational randomization is sufficiently large.[1,2] The mismatch of ionic radii, atomic masses, and valence states among the large number of elements gives rise to significant lattice distortions, and these randomly mixed elements interact electronically and/or magnetically through local distortions of the lattice.[3−6] High-entropy oxides (HEOs) are particularly interesting materials in fields that include magnetism, optics, and catalysis, as the properties of HEOs are often different from those expected based on simply averaging the properties of the end members, which is common for solid solutions with a smaller number of mixed elements.[1,7] Many of the fascinating properties of high entropy materials emerge from their unique combination of synergy and competition among the elements.

Such complex interactions among the large number of constituent elements can be seen in the band structures of high entropy materials. For example, in RuRhPdAgOsIrPtAu, new electronic states emerge from the metal energy levels decreasing in degeneracy.[8] In the rare-earth HEO $(Ce,Gd,La,Nd,Pr,Sm,Y)O_{2-\delta}$,[9] the band gap decreases by more than 1 eV relative to the parent compound, CeO_2. Entropy stabilization also allows HEOs to accommodate a large concentration of oxygen vacancies, which, in tandem with lattice distortions brought on by the range of cation sizes, can support unusual oxidation states, such as Pr^{4+} in $(Ce,Gd,La,Nd,Pr,Sm,Y)O_{2-\delta}$. In addition, the large number of constituent metals can lead to a shift in orbital energies. One representative example is the recently reported HEO spinel $(Fe,Co,Ni,Cu,Zn)Al_2O_4$, which exhibits a significant band gap narrowing relative to the parent phases.[10] Such a band

Received: February 16, 2023
Published: May 10, 2023

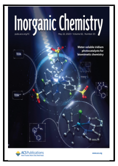

https://doi.org/10.1021/acs.inorgchem.3c00541

structure reconstruction can be attributed to the combined effect of the emergence of new t_{2g} and e_g states near the Fermi level due to the electronegativity differences of the mixed transition metals and the crystal field splitting of the high entropy phase adopting the smallest energy difference of the parent phases.[10]

Because of their unique band structures and the synergy of mixed elements, HEOs can exhibit unique properties that are superior to those of their end members, including both bulk properties such as thermal conductivity, mechanical strength, and ionic conductivity, and surface properties such as catalytic activity.[1−3,5] The superior catalytic activities of high-entropy materials, in particular, indicate that the mixed metal sites that comprise them also persist at the surface and advantageously impact surface properties. The complex active sites that emerge from the random combinations of the five metals have been shown to be advantageous in a wide range of catalytic reactions.[1] Of specific interest for HEOs is the oxygen evolution reaction (OER), which is the oxidation half reaction of overall water splitting. Under alkaline conditions, non-precious 3d transition-metal compounds containing Fe, Ni, and/or Co are often good OER catalysts that make them attractive for applications in fuel cells and batteries;[11] related HEOs sometimes outperform the single-metal oxide compounds and can sometimes have higher durability as well.[1,12,13]

Most existing HEOs adopt the rocksalt and spinel crystal structures, as there are many elements which will adopt these structures and thus can be reasonably expected to alloy. It is therefore important to synthesize and characterize additional HEO materials that span different families of crystal structures, given the importance of both composition and crystal structure on band structure and properties. Here, we report the synthesis and characterization, as well as optical, magnetic, and catalytic properties, of two HEO materials. These properties, which are most relevant to our chosen systems, were investigated to probe the physical properties that emerge from such materials and to put them into context with the larger field of HEO materials. A^6WO_4 (A = Mn, Fe, Co, Ni, Cu, and Zn) is a high-entropy tungsten oxide that adopts the monoclinic wolframite crystal structure and is a narrow band-gap antiferromagnet. $B_2^5Mo_3O_8$ (B = Mn, Fe, Co, Ni, and Zn) is a high-entropy molybdenum oxide that adopts a hexagonal crystal structure and is a semi-metallic paramagnet. This study focuses on compounds containing equimolar ratios of the A and B cations, as this ratio maximizes entropy stabilization and provides a starting point for future efforts to tune properties through compositional modifications. Computational predictions suggested that the parent phases of these two families of materials would show catalytic activity for the OER due to the formation of stable bonds and structures under OER conditions for tungsten and molybdenum oxides.[14,15] Here, we experimentally confirm that the OER activities of the HEOs are superior to those of their parent phases while also offering good durability at a current density of 10 mA/cm^2. We also find that A^6WO_4 exhibits long-range antiferromagnetic (AFM) order and lacks a band gap in the visible region, which sharply contrasts the corresponding properties of their parent phases, which are semiconductors exhibiting either AFM or non-magnetic behavior. $B_2^5Mo_3O_8$ is paramagnetic and appears to be a narrow band gap semiconductor, analogous to the single metal parent phases.

■ RESULTS AND DISCUSSION

Synthesis and Characterization. A^6WO_4 (A = Mn, Fe, Co, Ni, Cu, and Zn) and $B_2^5Mo_3O_8$ (B = Mn, Fe, Co, Ni, and Zn) were synthesized by direct combination of the constituent oxides in stoichiometric amounts at 900 and 1100 °C, respectively. Powder X-ray diffraction (PXRD) data, shown in Figure 1, confirm the formation of products consisting of a single crystalline phase with no evidence of bulk phase segregation. Lattice parameters were modified from those of the zinc end members,[16,17] monoclinic $ZnWO_4$ and hexagonal $Zn_2Mo_3O_8$ (Figure 1, Tables S1 and S2). A satisfactory fit of the tungstate A^6WO_4 HEO was achieved. For the molybdate $B_2^5Mo_3O_8$ HEO, there was an intensity mismatch that could be partially accounted for by including the preferred orientation (44%) of crystallites along the 010 plane in the model.

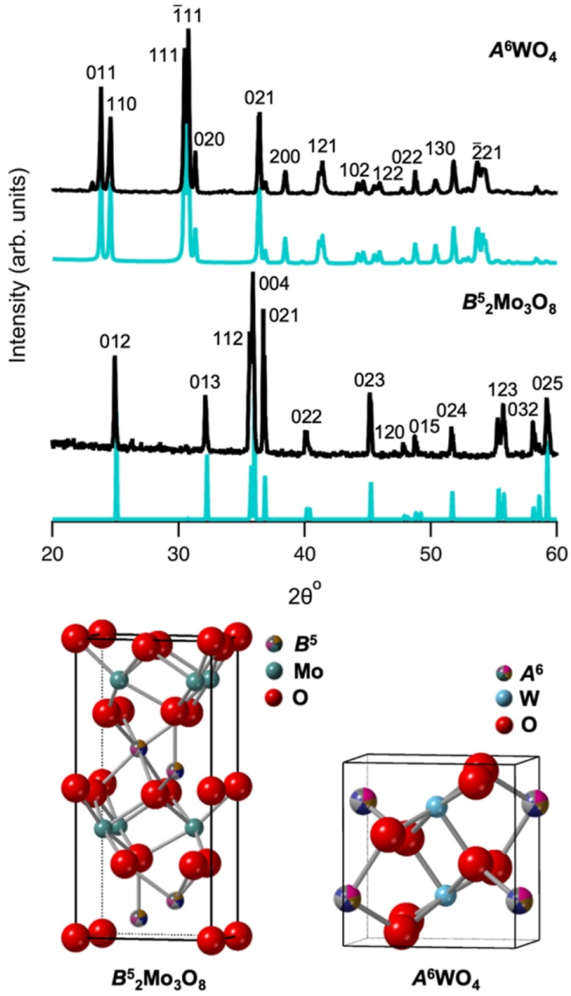

Figure 1. Experimental (black) and simulated (blue) powder XRD patterns of the A^6WO_4 and $B_2^5Mo_3O_8$ HEOs, along with their crystal structures.

The parent phases that are known in the literature[16,18−20] were also synthesized for comparison; PXRD data confirming their formation are shown in Figure S1. Unfortunately, as previously observed,[16] $Ni_2Mo_3O_8$ could only be formed as a minor phase, with $NiMoO_4$ forming as the major product. Therefore, this parent compound was not examined in this study. For the tungstate A^6WO_4 HEO, six metals (Mn, Fe, Co,

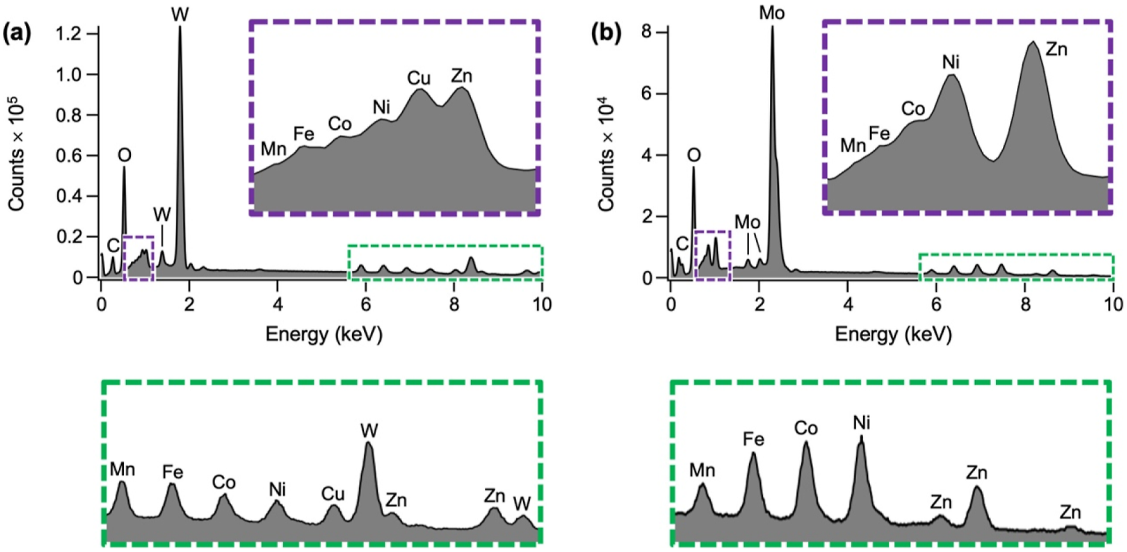

Figure 2. SEM−EDX spectra for powders of (a) A^6WO_4 and (b) $B_2{}^5Mo_3O_8$. Both have approximately equimolar amounts of the 3d transition metals, as well as the expected ratios to tungsten and molybdenum. Expanded regions, indicated in purple and green boxes, confirm the presence of the 3d transition elements.

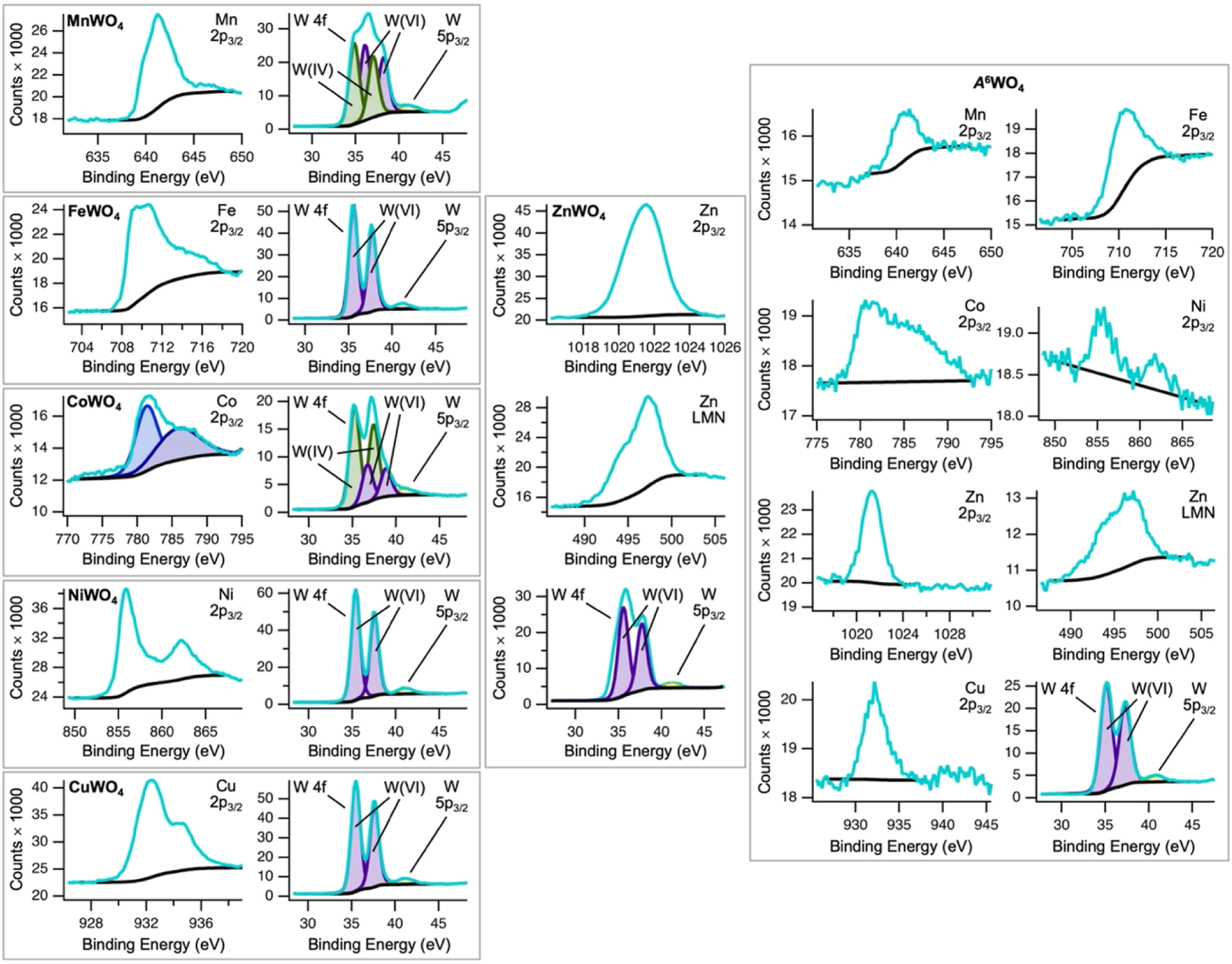

Figure 3. High-resolution XPS spectra for the elements present in A^6WO_4 and in the AWO_4 parent phases.

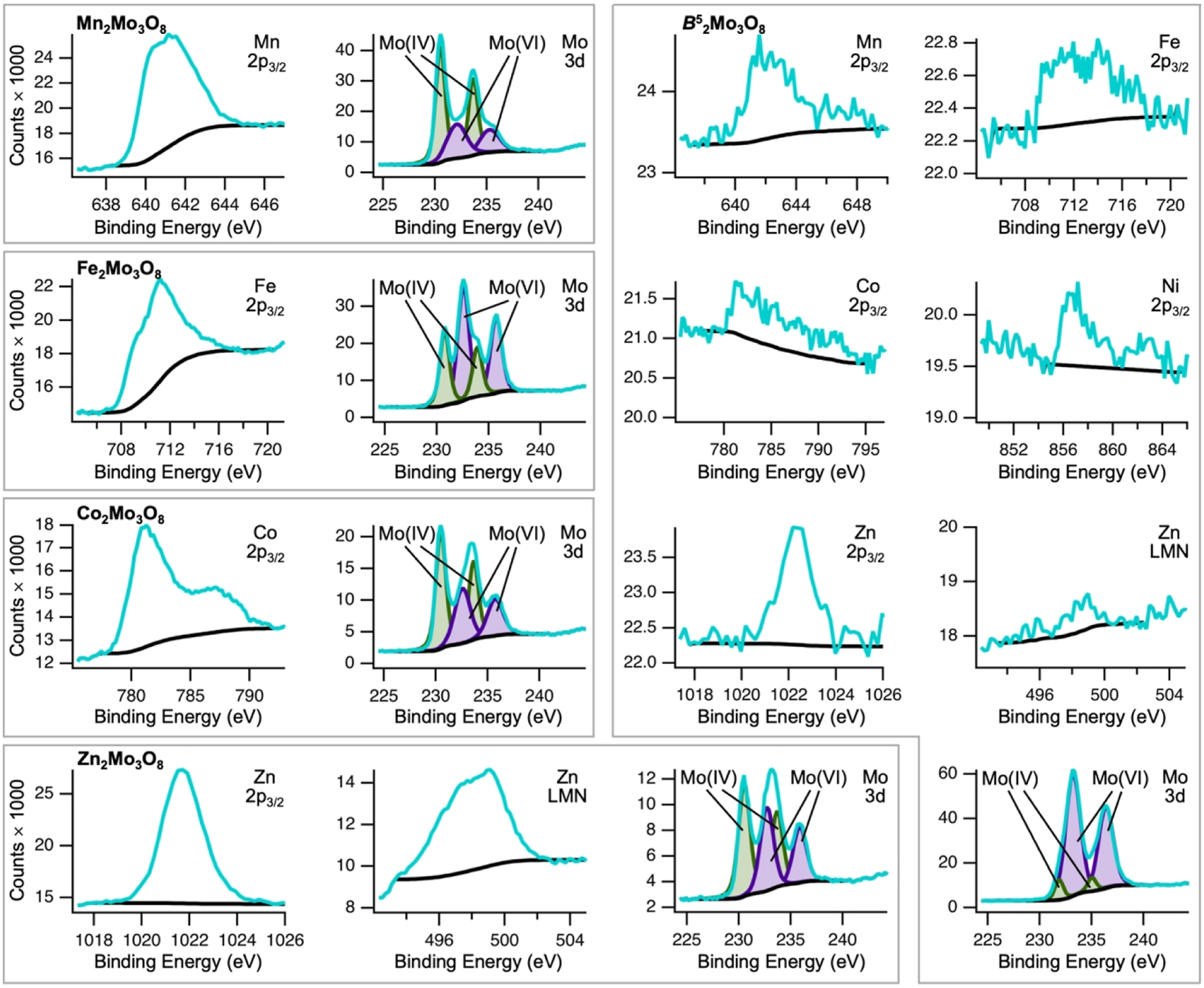

Figure 4. High-resolution XPS spectra for the elements present in $B_2{}^5Mo_3O_8$ and in the $B_2Mo_3O_8$ parent phases.

Ni, Cu, and Zn) can be incorporated in equimolar amounts, and all six AWO_4 parent phases can be synthesized. For the molybdate $B_2{}^5Mo_3O_8$ HEO, the copper parent phase $Cu_2Mo_3O_8$ does not form, and we find that it also cannot be incorporated into the HEO. Therefore, unlike for the high-entropy tungstate that can accommodate six 3d transition metals, we were only able to incorporate five 3d transition metals (Mn, Fe, Co, Ni, and Zn) into the high-entropy molybdate. While the molybdenum oxides can also exist as $BMoO_4$ phases, the parent phases adopt different crystal structures at ambient pressure.[21] $Zn_{1-x}Cu_xMoO_4$ solid solutions can be formed, but they do not adopt the same crystal structure as $MnMoO_4$, $FeMoO_4$, $CoMoO_4$, and $NiMoO_4$.[22] Furthermore, both $FeMoO_4$ and $CuMoO_4$ are reported to have three accessible phases.[23−25] For $FeMoO_4$, there exists a low-temperature, low-pressure monoclinic form that is isostructural with the low-temperature forms of $CoMoO_4$ and $NiMoO_4$, a high-temperature form that is isostructural with $MnMoO_4$ and $MgMoO_4$, and a unique high-pressure form.[23] While $CuMoO_4$ also forms a low-pressure low-temperature phase, a high-temperature phase, and a high-pressure phase, only the low-pressure low-temperature phase is structurally similar to another member of the family, $ZnMoO_4$.[25] $CoMoO_4$ and $NiMoO_4$ each have been reported to form in two related phases.[26] These phases are differentiated by the molybdenum coordination, which is octahedral in the low-temperature phase and tetrahedral at high temperatures. The wide range of crystal structures that exist among the different parent phases led to an inability to synthesize a high-entropy $BMoO_4$ compound (B = Mn, Fe, Co, Ni, Cu, and Zn), as bulk phase segregation resulted from all attempts.

SEM−EDX mapping of powders of A^6WO_4 and $B_2{}^5Mo_3O_8$ revealed a homogeneous distribution of all constituent elements (Figures 2 and S2), with the A and B metals present in nearly equimolar amounts (within experimental error) throughout the samples. For A^6WO_4, the six A metals were each present at 3 atomic percent (for a combined total of 18 atomic percent), while tungsten was present at 15 atomic percent, close to the expected 1:1 A/W ratio. For $B_2{}^5Mo_3O_8$, the five B metals were each present at ∼2 atomic percent (for a combined total of 10 atomic percent), and molybdenum was present at 14 atomic percent, corresponding well with the expected 2:3 B/Mo ratio. By EDX, the remainder of the sample consisted of carbon, nitrogen, and oxygen.

Surface Characterization by X-ray Photoelectron Spectroscopy. X-ray photoelectron spectroscopy (XPS) was used to analyze the compositions and oxidation states of the surfaces of both the parent phases and the HEOs (Figure 3). We began by studying the tungsten compounds. Considering simple charge balancing, if tungsten is in a formal 6+ oxidation state, the 3d transition metals would be expected to adopt a 2+ oxidation state on average. However, it appears that the distribution of oxidation states is more complex in both the HEOs and in the parent compounds. Comparing the peak positions of the 3d transition metals in A^6WO_4 and in the parent compounds, the binding energy of the $2p_{3/2}$ peak of manganese in A^6WO_4, which is 640.4 eV, indicates a 2+ oxidation state, whereas in $MnWO_4$, the same peak is found at 641.2 eV, which is more indicative of Mn^{3+}.[27] For iron in A^6WO_4, the $2p_{3/2}$ peak at 710.2 eV matches most closely with previous reports of Fe_3O_4, which contains both Fe^{2+} and Fe^{3+}, while iron in $FeWO_4$, which has a binding energy of 709.4 eV, appears to match best with FeO that has exclusively Fe^{2+}.[27] For cobalt in A^6WO_4, the $2p_{3/2}$ peak at 780.6 eV is attributed to Co^{2+} due to a close match with reported values.[27] In $CoWO_4$, both the cobalt $2p_{3/2}$ and the plasmon loss peak could be fit, with binding energies of 780.3 and 785.8 eV, respectively, as observed for CoO, which contains Co^{2+}.[27] The $2p_{3/2}$ peak for nickel in both A^6WO_4 and $NiWO_4$ has a binding energy of 855.8 eV, which is commensurate with Ni^{2+}.[27] The copper $2p_{3/2}$ peak, with a binding energy of 932.2 eV in A^6WO_4 and 932.3 eV in $CuWO_4$, corresponds to Cu^{1+}.[28] The zinc oxidation state was determined by the Auger parameters, as these are more sensitive to zinc oxidation states.[28] The Auger parameter for A^6WO_4 is 2011.8 eV, whereas in $ZnWO_4$ it is 2011.0 eV; both values are indicative of Zn^{2+}.[28]

Given the XPS analysis of the 3d transition-metal oxidation states above, we turned to the tungsten oxidation states (Figure 3). For A^6WO_4, the tungsten $4f_{7/2}$ and $4f_{5/2}$ peaks at 35.1 and 37.3 eV indicate that tungsten is present as W^{6+}.[29] Considering the oxidation states of the 3d transition metals in A^6WO_4 and that tungsten is present exclusively as W^{6+}, the presence of Cu^{1+} rather than Cu^{2+} is consistent with the presence of Fe^{3+}, which balances charge. In $MnWO_4$, both W^{6+} and W^{4+} are present, based on the $4f_{7/2}$ peaks at 36.1 and 38.8 eV and the $4f_{5/2}$ peaks at 38.2 and 37.0 eV, respectively.[29] Considering that the manganese oxidation state in $MnWO_4$ was most consistent with Mn^{3+} and our spectrum matches previous reports of $MnWO_4$,[30] the presence of W^{4+} is not unexpected. In $FeWO_4$, tungsten is present exclusively as W^{6+} ($4f_{7/2}$ and $4f_{5/2}$ peaks at 35.5 and 37.7 eV, respectively), which is in agreement with the observation of Fe^{2+} in this compound. For $CoWO_4$, both W^{6+} and W^{4+} are observed, based on the $4f_{7/2}$ peaks at 36.7 and 35.3 eV, and the $4f_{5/2}$ peaks at 38.9 and 37.4 eV. $NiWO_4$ and $CuWO_4$ contain only W^{6+}, with the $4f_{7/2}$ peaks at 35.4 and 37.5 eV and the $4f_{5/2}$ peaks at 35.5 and 37.6 eV, respectively. $ZnWO_4$ contains only W^{6+} with the $4f_{7/2}$ and $4f_{5/2}$ peaks at 35.3 and 37.4 eV, respectively. Regarding the oxidation states, it is important to note that they correspond to those that are present on the surface. While we used finely ground powder to access as much of the bulk of the material as possible, we cannot rule out the possibility that these oxidation states could be exclusive to the surfaces.

Analogous to A^6WO_4, we also used XPS to identify the surface oxidation states of the molybdenum HEO, $B_2{}^5Mo_3O_8$, as well as of the molybdenum parent compounds (Figure 4). Given the formula $B_2Mo_3O_8$, one would expect the 3d metals and molybdenum to adopt oxidation states of 2+ and 4+, respectively. However, as for the tungsten compounds, the oxidation state distributions are much more complex. The Mn $2p_{3/2}$ binding energies for $Mn_2Mo_3O_8$ and $B_2{}^5Mo_3O_8$ are 641.1 and 641.5 eV, respectively, which are both indicative of Mn^{3+}.[27] The Fe $2p_{3/2}$ binding energy in $Fe_2Mo_3O_8$ is 711.1 eV, as would be expected for a mixture of Fe^{2+} and Fe^{3+}, as in Fe_3O_4.[27] The overall iron signal is low in both $Fe_2Mo_3O_8$ and $B_2{}^5Mo_3O_8$; for $B_2{}^5Mo_3O_8$, the iron signal was too low to quantify. This low iron signal is attributed to post-synthesis etching during workup to remove a MoO_3 impurity as well as the overlap of the Fe $2p_{3/2}$ peak with the cobalt Auger peak. The Co $2p_{3/2}$ peak at 783.5 eV for $B_2{}^5Mo_3O_8$ and at 781.2 eV for $Co_2Mo_3O_8$ both match with previous reports of cobalt hydroxides, $Co(OH)_2$ and CoOOH, respectively.[27] This suggests that $B_2{}^5Mo_3O_8$ contains Co^{2+} while $Co_2Mo_3O_8$ contains Co^{3+}. While $Ni_2Mo_3O_8$ could not be synthesized, the Ni $2p_{3/2}$ peak in $B_2{}^5Mo_3O_8$ has a binding energy of 857.1 eV, which corresponds to Ni^{2+}.[27] Zinc, which has an Auger parameter of 2010.0 eV, for both $Zn_2Mo_3O_8$ and the HEO, is present as Zn^{2+}.[28] All the molybdenum compounds show mixed Mo^{4+} and Mo^{6+} oxidation states. For $B_2{}^5Mo_3O_8$, molybdenum $3d_{5/2}$ and $3d_{3/2}$, the simple doublet peaks at 233.2 and 236.4 eV, match with previous reports of Mo^{6+}.[31,32] The $3d_{5/2}$ and $3d_{3/2}$ peaks at 231.9 and 235.0 eV correspond to Mo^{4+}. The propensity to form MoO_3 as an impurity does not make it surprising that Mo^{6+} is favored at the surface, even though Mo^{4+} would be expected, assuming the 3d metals generally adopt a 2+ oxidation state.

Magnetic Properties. For the tungstate AWO_4 parent compounds, $ZnWO_4$ is known to be paramagnetic, while the others are known to exhibit long-range AFM ordering with Néel temperatures (T_N) of 13 K for $MnWO_4$, 24 K for $CuWO_4$, 55 K for $CoWO_4$, 62 K for $NiWO_4$, and 72 K for $FeWO_4$.[18,19] We find that A^6WO_4 also exhibits long-range AFM ordering with T_N = 30 K (Figure 5a). This transition temperature is 15 K below the average T_N of 45.2 K for the AFM parent compounds. This result, together with the observation that A^6WO_4 displays only a single AFM transition, indicates that despite the competing magnetic interactions in the HEO phase, at this temperature they can achieve long-range ordering. The observation of a single AFM transition also suggests that the mixing of the magnetic 3d transition metals at the A site is homogeneous, as multiple magnetic transitions would be present if there were phase separation due to clustering of different 3d elements.

Unlike the tungstate parent compounds, which are all AFM except for $ZnWO_4$, the $B_2Mo_3O_8$ molybdates include both AFM and ferromagnetic compounds, except for $Zn_2Mo_3O_8$, which is paramagnetic. $Fe_2Mo_3O_8$, $Co_2Mo_3O_8$, and $Ni_2Mo_3O_8$ are AFM with T_N = 60, 41, and 6 K, respectively,[33,34] while $Mn_2Mo_3O_8$ is ferromagnetic with a Curie temperature (T_c) of 42 K.[33,35] In contrast, the $B_2{}^5Mo_3O_8$ HEO was found to be paramagnetic (Figure 5b). This observation suggests that the low population of magnetic elements on the B sites, together with the competing magnetic correlations favored by the different metals, makes the exchange interaction-mediated magnetic ordering unstable. This instability leads to a loss of long-range magnetic order. To summarize, the magnetic data show that there is one magnetic transition for A^6WO_4 and a lack of magnetic transitions for $B_2{}^5Mo_3O_8$. This lends confidence to the idea that there is not phase segregation, because if the parent phases segregated out, their individual magnetic transitions would be observed.

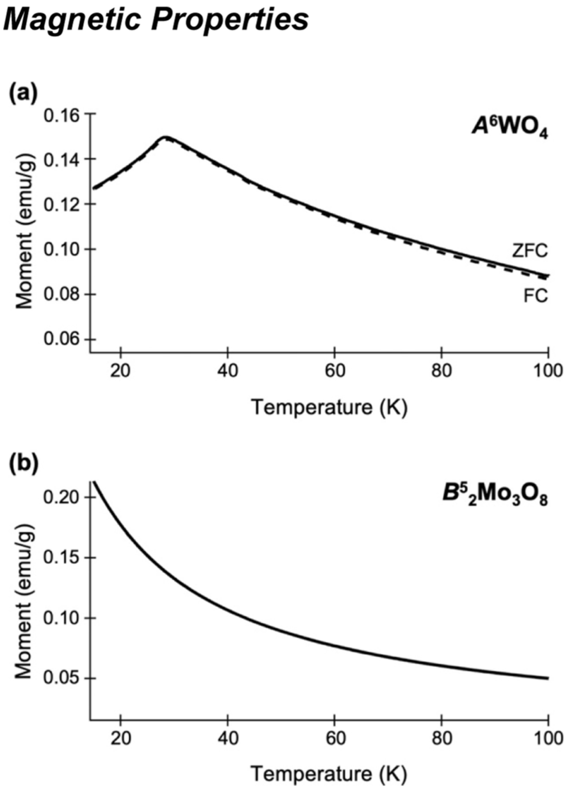

Figure 5. Magnetization data for (a) A^6WO_4, which is AFM with T_N = 30 K, and (b) $B_2{}^5Mo_3O_8$, which is paramagnetic.

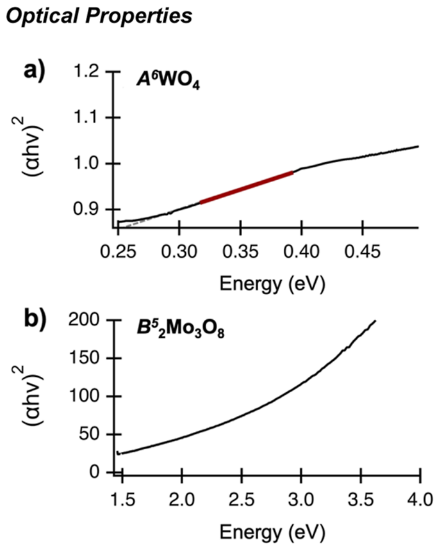

Figure 6. Tauc plot derived from (a) infrared (IR) spectroscopy and linear fit band gap determination for A^6WO_4. (b) Tauc plot derived from UV−vis spectroscopy for $B_2{}^5Mo_3O_8$.

Optical Properties. All of the tungstate parent compounds that we synthesized are semiconductors with measured band gaps (E_g) ranging from 2.6 to 3.8 eV: 2.5 eV for $MnWO_4$, 2.6 eV for $FeWO_4$, 2.7 eV for $CoWO_4$, 3.1 eV for $NiWO_4$, 2.3 eV for $CuWO_4$, and 3.8 eV for $ZnWO_4$ (Figure S3). These band gap measurements fall within 0.2 eV of previously published band gaps for all compounds.[36−42] In contrast, the high-entropy tungstate A^6WO_4 was black and had no observable band gap down to 1.5 eV, based on UV−visible (UV−vis) absorption spectroscopy. FT-IR measurements, which can provide evidence of lower−energy transitions associated with narrow band gaps,[43] revealed a transition at 0.24 eV, when transformed into a Tauc plot. The existence of a narrow band gap indicates that this material is a degenerate semiconductor (Figure 6a). The striking difference in band gaps between A^6WO_4 and all of the parent compounds is consistent with the previously observed band structure reconstruction and narrowing in other transition metal HEOs, such as $A^5Al_2O_4$, and rare earth HEOs, such as $(Ce,Gd,La,Nd,Pr,Sm,Y)O_{2-\delta}$,[9,10] as discussed above. In contrast to the tungstates, all of the molybdate parent compounds have a black color, as previously reported,[16] with no observable band gaps in the visible or near-IR range (Figure 6b). A band gap in a Tauc plot is identified by a linear region that is then extrapolated to the *x*-axis. A weak optical transition that is present in $Mn_2Mo_3O_8$ and $Zn_2Mo_3O_8$ is attributable to a MoO_3 impurity, which also appears in the powder XRD patterns for these parent compounds. Similar to the parent compounds, $B_2{}^5Mo_3O_8$ appears black, and its Tauc plot does not have a true linear range.

Electrocatalytic Properties. HEOs that incorporate 3d transition metals have emerged as materials of interest for catalyzing the OER under alkaline conditions.[1] Furthermore, the inclusion of tungsten or molybdenum in ternary oxide compounds has been proposed to be important for achieving catalytic durability for this reaction.[15] We therefore investigated the catalytic viability of the tungstate and molybdate HEOs, as well as their parent compounds, for the OER and found that many of them indeed are active OER catalysts. All materials were drop-cast on glassy carbon electrodes and tested in 1 M KOH.

We found that $MnWO_4$, $FeWO_4$, $CuWO_4$, and $ZnWO_4$ were not active OER catalysts, but both $CoWO_4$ and $NiWO_4$ were able to catalyze the OER in 1 M KOH. $CoWO_4$ and $NiWO_4$ reached a current density of 10 mA/cm^2, as normalized to geometric surface area, at potentials of 1.66 and 1.72 V vs RHE, respectively (Figure S8). The high-entropy analogue, A^6WO_4, was a more active OER catalyst based on comparable metrics, reaching a current density of 10 mA/cm^2 at a potential of 1.59 V vs RHE. Moving to the molybdates, we similarly found that $Mn_2Mo_3O_8$, $Fe_2Mo_3O_8$, $Ni_2Mo_3O_8$, and $Zn_2Mo_3O_8$ were not active OER catalysts. $Co_2Mo_3O_8$ performed comparably to $CoWO_4$, producing a current density of 10 mA/cm^2 at 1.67 V. Based on similar current−potential metrics, $B_2{}^5Mo_3O_8$ performed similarly, achieving a current density of 10 mA/cm^2 at 1.64 V (Figure S8). However, when current was normalized to the electrochemically active surface area, which better accounts for the total surface area available for catalysis to occur, only A^6WO_4 and $B_2{}^5Mo_3O_8$ reached the benchmark current density of 10 mA/cm^2 in the measured potential range of 1.2−1.75 V vs RHE (Figures 7, S8, and S9), achieving current densities of 10 mA/cm^2 at overpotentials of 480 and 410 mV, respectively. These values are on par with previous literature reports for relevant single-metal oxides, such as CoO_x and NiO_x, which require overpotentials of 430 and 420 mV, respectively, to reach a current density of 10 mA/cm^2.[44] As expected for bulk powders that have low surface areas, their performance does not reach that of the best and highest surface-area OER catalysts in alkaline electrolytes, including nickel-iron hydroxide compounds, which can reach current densities of 10 mA/cm^2 at an overpotential of less than 250 mA.[45,46] Nonetheless, the HEOs offer a notable improvement relative to the catalytic activities of their parent compounds,

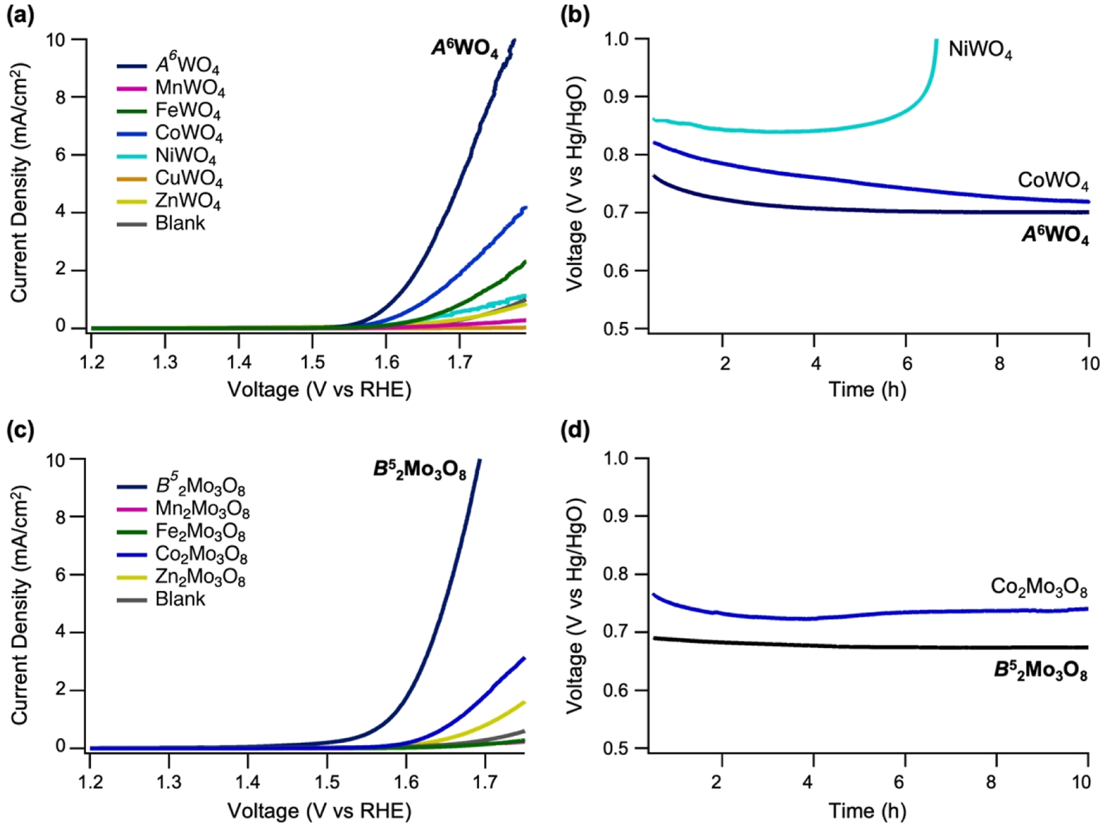

Figure 7. Electrochemical performance for the OER, of (a) A^6WO_4 and the tungstate parent compounds and (c) $B_2^5Mo_3O_8$ and the molybdate parent compounds, as shown by linear sweep voltammetry, with current normalized to electrochemical active surface area. Initial stability was assessed by holding the most active (b) tungstates and (d) molybdates at a current density of 10 mA/cm^2 for 10 h.

having comparable morphologies, surface areas, and preparation methods, and further development through composition modulation or nanostructuring could further improve their performance metrics.[47,48]

Over a 10 h initial stability screening test at 10 mA/cm^2, both $CoWO_4$ and A^6WO_4 exhibited stable performance based on the observation that there was not a significant increase in the voltage needed to maintain this current, nor was there gross dissolution of the catalyst, as observed by inductively coupled plasma analysis (ICP, Table S3). In contrast, $NiWO_4$ failed at 6 h, as observed by a rapid increase in the voltage. This behavior can be attributed to catalyst degradation and subsequent dissolution into the electrolyte, as no catalyst could be visually observed on the electrode surface after 6 h. For the molybdenum oxides, only $B_2^5Mo_3O_8$ and $Co_2Mo_3O_8$ were able to reach a current density of 10 mA/cm^2 in the measured potential range of 1.2−1.75 V vs RHE. Both materials were stable for the 10 h test (Figure 7b,d). For $B_2^5Mo_3O_8$, ICP analysis confirmed that there was no gross dissolution of the catalyst (Table S3). Based on these measurements, both A^6WO_4 and $B_2^5Mo_3O_8$ are active OER catalysts in KOH and perform better than their OER-active parent compounds, based on their overpotentials required to achieve a surface area normalized current density of 10 mA/cm^2. Importantly, neither show signs of significant dissolution at these applied potentials over a 10 h window.

XPS was used to compare the surface composition and oxidation states of A^6WO_4 and $B_2^5Mo_3O_8$ before and after catalysis (Figures S10 and S11). As expected, many of the 3d transition metals on the surfaces of the HEO compounds oxidized after OER catalysis in KOH. For A^6WO_4, manganese oxidized to Mn^{3+}, based on the Mn $2p_{3/2}$ binding energy of 641.2 eV,[27] and iron oxidized to Fe^{3+}, based on the Fe $2p_{3/2}$ binding energy of 711.4 eV that matches previous reports of FeOOH.[27] The Co $2p_{3/2}$ binding energy of 779.8 eV is close to that observed for Co_3O_4,[27] indicating the possibility of mixed Co^{2+}/Co^{3+}. The Ni $2p_{3/2}$ binding energy of 854.0 eV has previously been reported for NiOOH and indicates Ni^{3+}.[27] The Cu $2p_{3/2}$ binding energy of 933.2 eV corresponds to Cu^{2+},[28] which indicates oxidation from the as-synthesized compound, which had Cu^{1+}. The Zn Auger parameter of 2010.0 eV is consistent with Zn^{2+}, indicating no change in oxidation state after catalysis, as expected for zinc.[28] The increase in oxidation state for the 3d transition metals in A^6WO_4 is consistent with the oxidizing environment of the electrolyte and the applied bias during catalysis. Tungsten largely remained as W^{6+}, based on the $4f_{7/2}$ and $4f_{5/2}$ peaks at 34.7 and 36.9 eV. There were a pair of small peaks at 32.5 and 34.9 eV, which are attributed to K 3s.

For $B_2^5Mo_3O_8$ after catalysis, the binding energy of 641.7 eV for Mn $2p_{3/2}$, which corresponds to Mn^{4+}, indicates oxidation from the as-synthesized HEO, which had Mn^{3+}.[27] The low-signal peak for iron, while still present, is once again too broad due to the overlap with the cobalt Auger peak to confidently identify the peak position and oxidation state. The Co $2p_{3/2}$ peak at 779.9 eV is consistent with Co^{2+}/Co^{3+}, which indicates partial oxidation relative to the as-synthesized compound, containing only Co^{2+}. The Ni $2p_{3/2}$ binding energy of 855.0 eV, which corresponds to Ni^{3+}, indicates oxidation relative to the Ni^{2+} that was present before catalysis. The mixed $Mo^{4+}/$

Mo^{6+} species that were present in as-synthesized $B_2{}^5Mo_3O_8$ remain present after catalysis, based on the observation of the molybdenum $3d_{5/2}$ peaks at 230.0 and 231.6 eV and the $3d_{3/2}$ peaks at 233.16 and 234.8 eV. As for A^6WO_4, surface oxidation arises from the oxidizing electrochemical conditions during catalysis.

■ CONCLUSIONS

We reported the synthesis and characterization of two high-entropy mixed-metal oxides, the tungstate A^6WO_4 (A = Mn, Fe, Co, Ni, Cu, and Zn) and the molybdate $B_2{}^5Mo_3O_8$ (B = Mn, Fe, Co, Ni, and Zn), which expand the phase space of HEO materials. Key magnetic, optical, and electrocatalytic properties of these high-entropy compounds were explored to gain an understanding of how they compared to their parent compounds, and several notable findings were uncovered. XPS confirmed the presence of all elements at the surface. For A^6WO_4, XPS showed the presence of W^{6+} and A^{2+} except for iron and copper, which were $Fe^{2+/3+}$ and Cu^+, respectively. In contrast, $B_2{}^5Mo_3O_8$ contained Mo^{4+} and Mo^{6+} with Mn^{3+}, $Fe^{2+/3+}$, Co^{2+}, Ni^{2+}, and Zn^{2+}. The long-range magnetic ordering that is present in most of the single-metal $B_2Mo_3O_8$ parent compounds was lost in the high-entropy $B_2{}^5Mo_3O_8$ compound, while A^6WO_4 maintained the AFM ordering that is present in all of its parent compounds, except $ZnWO_4$. The differences between the high-entropy tungstate and molybdate may be because five of the six metals in A^6WO_4 contribute to AFM ordering, which leads to less magnetic dilution than in $B_2{}^5Mo_3O_8$. While none of the molybdates had observable band gaps, the optical properties of A^6WO_4 were interesting. The single-metal parent compounds were semiconductors, while A^6WO_4 had a significantly narrowed band gap. This observation highlights the possibility of electronic structure changes caused by high-entropy mixing. Due to the emerging interest in both HEOs and oxides of tungsten and molybdenum as active and durable catalysts for the OER, both A^6WO_4 and $B_2{}^5Mo_3O_8$ were considered candidate catalysts and found to exhibit enhanced activity relative to the parent compounds based on the overpotential required to achieve a benchmark surface area normalized current density. Both HEOs showed stable activity during a 10 h constant current test. Both HEOs are therefore interesting materials for their potential physical and chemical properties, as well as their contribution toward identifying and understanding the structure−property relationship in HEOs that is anticipated to lead to the future development of HEO materials for targeted magnetic, optical, and catalytic properties and applications.

■ EXPERIMENTAL SECTION

Synthesis of Tungstate Compounds. The tungstate compounds $MnWO_4$, $FeWO_4$, $CoWO_4$, $NiWO_4$, $CuWO_4$, $ZnWO_4$, and A^6WO_4 were made using a modification of a previously reported solid-state synthesis of $NiWO_4$.[49] The following powders were first weighed out in appropriate stoichiometric ratios: CuO (Sigma-Aldrich, 99.0%), $MnCO_3$ (Sigma-Aldrich, 99.9%), NiO (Sigma-Aldrich, 99.8%), ZnO (Sigma-Aldrich, 99.0%), CoO (Alfa Aesar, 95%), FeO (Sigma-Aldrich, 99.7%), and WO_3 (Alfa Aesar, 99.8%). For the parent compounds, generally a 1:1 molar ratio of the 3d transition-metal oxide/carbonate to WO_3 was used. For $MnCO_3$, NiO, and CoO, a 5% excess (by mass) was used. For A^6WO_4, which contained all six 3d transition metals, each oxide/carbonate was used in a 1/6th molar ratio relative to tungsten, for a stoichiometry of $Mn_{0.167}Fe_{0.167}Co_{0.167}Ni_{0.167}Cu_{0.167}Zn_{0.167}WO_4$. Specific amounts for each compound are given in the Supporting Information (Table S4). The weighed powders for each compound were ground with an agate mortar and pestle, pressed into pellets, and then heated in a furnace in air at 900 °C for 12 h, ramping at 200 °C/h. For $FeWO_4$, the synthesis was performed in a sealed evacuated quartz tube because, in air, Fe_2O_3 formed as the major product. The pellets were reground, and their formation was confirmed via PXRD at room temperature.

Synthesis of Molybdate Compounds. The molybdate compounds $Mn_2Mo_3O_8$, $Fe_2Mo_3O_8$, $Co_2Mo_3O_8$, $Zn_2Mo_3O_8$, and $B_2{}^5Mo_3O_8$ were made using a solid-state method based on a published synthesis of $Fe_2Mo_3O_8$ and $Zn_2Mo_3O_8$.[50] The following powders were first weighed out in appropriate stoichiometric ratios: CoO (Alfa Aesar, 95%), NiO (Sigma-Aldrich, 99.8%), MoO_3 (Matheson Coleman and Bell, 99.5%), Mo (Sigma-Aldrich, 99.94%, mesh < 150 μm), Fe_2O_3 (Sigma-Aldrich, 99.99%), ZnO (Sigma-Aldrich, 99%), and Mn_3O_4 (Sigma-Aldrich, 97%). A 1:2:1 molar ratio of 3d transition-metal oxide to MoO_3 to Mo was used to restrict the amount of oxygen available for the reaction. For $B_2{}^5Mo_3O_8$, which contained all five 3d transition metals, each corresponding oxide was used in a 2/5th molar ratio relative to the formula $B_2Mo_3O_8$. Specific amounts for each compound are given in the Supporting Information (Table S4). The weighed powders for each compound were ground with an agate mortar and pestle, pressed into pellets, and then sealed in quartz tubes evacuated to 10^{-4} Torr. Each tube was heated at 700 °C for 24 h and then at 1100 °C for 2 h, ramping at 200 °C/h. The pellets were reground and their formation was confirmed via PXRD at room temperature.

Powder X-ray Diffraction. Powder XRD data were collected on a Malvern Panalytical Empyrean diffractometer. The instrument was equipped with a copper source and operated at a voltage of 45 keV and a power of 40 kW. Powder XRD patterns were obtained using reflection mode and a PIXcel 3D detector.

Scanning Electron Microscopy. Scanning electron microscopy with energy dispersive X-ray spectroscopy (SEM−EDX) was used to determine the elemental composition and distribution of elements in the bulk powders. Data were collected on an ESEM Q250 with a tungsten source. The instrument was operated at 7 keV under ultra-high vacuum. Imaging and mapping of elemental composition were done utilizing secondary electrons. For elemental mapping, an EDS Bruker AXS detector was used. Elemental maps were constructed on the Aztec software, which performed automatic peak integrations of the spectra to determine elemental composition as well as allowing visualization of the location of elements.

X-ray Photoelectron Spectroscopy. XPS were collected using a Physical Electronics VersaProbe II instrument equipped with a monochromatic Al Kα X-ray source ($h\nu$ = 1486.7 eV) and a concentric hemispherical analyzer. Charge neutralization was performed using both low-energy electrons (<5 eV) and argon ions. The binding energy axis was calibrated using sputter cleaned Cu (Cu $2p_{3/2}$ = 932.62 eV, Cu $3p_{3/2}$ = 75.1 eV) and Au (Au $4f_{7/2}$ = 83.96 eV) foils. Peaks were charge referenced to the CH_x band in the carbon 1s spectra at 285 eV. Measurements were made at a takeoff angle of 45° with respect to the sample surface plane. This resulted in a typical sampling depth of 3−6 nm (95% of the signal originated from this depth or shallower).

Magnetic Measurements. Magnetic measurements were conducted on a Quantum Design vibrating sample superconducting quantum interference device (SQUID) magnetometer. A field of 0.1 T was used for measurements, conducted from 100 to 15 K under both field cooling and zero field cooling histories. A brass holder, with a plastic powder sample cup, was used for the measurements.

Spectroscopic Measurements. UV−vis absorption spectroscopy was collected on a Shimazu UV−vis spectrometer equipped with a Harrick Praying Mantis Diffuse Reflection Accessory. Spectra were referenced to a background of potassium bromide (Sigma-Aldrich, spectroscopy quality). A step size of 0.2 nm was used to scan from 1.5 to 4 eV. FTIR spectroscopy measurements were performed on a Bruker Vertex 80 spectrometer equipped with a Harrick Praying Mantis Diffuse Reflection Accessory and a liquid nitrogen-cooled mercury cadmium telluride detector. A total of 500 scans were averaged at a resolution of 6 cm^{-1}, and absorbance was calculated by referencing to an ozone-cleaned Labsphere Infragold target.

Electrochemical Measurements. All electrochemical measurements were conducted in 1 M KOH (VWR, 98%) using a rotating disk working electrode, a graphite rod counter electrode, and a mercury−mercury oxide reference electrode, which is a stable reference in base. The working electrode substrate was glassy carbon, polished to 1/4 μm smoothness by using diamond paste on a polishing cloth. Polishing was conducted at 9, 3, 1, 1/2, and 1/4 μm to ensure a smooth and clean surface. The electrode ink was made by sonicating 2 mg of the catalyst powder and 20 μL of Nafion perfluorinated resin in a solvent mixture of 400 μL of Nanopure water and 100 μL of isopropyl alcohol. Sonication was conducted for 1 h. Then, 20 μL of the catalyst ink was deposited on the glassy carbon electrode to maintain consistent catalyst loading and to ensure good contact between the electrode and catalyst. Potentials were applied utilizing a Gamry 1000b potentiostat.

■ ASSOCIATED CONTENT

Supporting Information

The Supporting Information is available free of charge at https://pubs.acs.org/doi/10.1021/acs.inorgchem.3c00541.

Additional XRD, SEM, UV−vis, XPS, and electrochemical data (PDF)

■ AUTHOR INFORMATION

Corresponding Authors

Zhiqiang Mao − *Department of Chemistry, The Pennsylvania State University, University Park, Pennsylvania 16802, United States; Department of Physics, The Pennsylvania State University, University Park, Pennsylvania 16802, United States;* orcid.org/0000-0002-4920-3293; Email: zim1@psu.edu

Raymond E. Schaak − *Department of Chemistry, The Pennsylvania State University, University Park, Pennsylvania 16802, United States; Department of Chemical Engineering and Materials Research Institute, The Pennsylvania State University, University Park, Pennsylvania 16802, United States;* orcid.org/0000-0002-7468-8181; Email: res20@psu.edu

Authors

Rowan R. Katzbaer − *Department of Chemistry, The Pennsylvania State University, University Park, Pennsylvania 16802, United States*

William M. Vincent − *Department of Chemistry, The Pennsylvania State University, University Park, Pennsylvania 16802, United States*

Complete contact information is available at: https://pubs.acs.org/10.1021/acs.inorgchem.3c00541

Author Contributions

The synthesis was performed by R.R.K. and W.M.V. under the advisement of R.E.S. and Z.M. All authors contributed to writing the manuscript.

Notes

The authors declare no competing financial interest.

■ ACKNOWLEDGMENTS

This work was primarily supported by the National Science Foundation through the Penn State Materials Research Science and Engineering Center (MRSEC) DMR-2011839. SEM, XRD, UV−vis, and XPS data were acquired at the Materials Characterization Lab of the Penn State Materials Research Institute. The authors thank Yingdong Guan for assistance with collecting the magnetic data and Dr. Jeff Shallenberger for his insight into the XPS analysis.

■ REFERENCES

(1) Sun, Y.; Dai, S. High-Entropy Materials for Catalysis: A New Frontier. *Sci. Adv.* **2021**, *7*, 1600.

(2) Musicó, B. L.; Gilbert, D.; Ward, T. Z.; Page, K.; George, E.; Yan, J.; Mandrus, D.; Keppens, V. The Emergent Field of High Entropy Oxides: Design, Prospects, Challenges, and Opportunities for Tailoring Material Properties. *APL Mater.* **2020**, *8*, 040912.

(3) Sarkar, A.; Wang, Q.; Schiele, A.; Chellali, M. R.; Bhattacharya, S. S.; Wang, D.; Brezesinski, T.; Hahn, H.; Velasco, L.; Breitung, B. High-Entropy Oxides: Fundamental Aspects and Electrochemical Properties. *Adv. Mater.* **2019**, *31*, 1806236.

(4) Witte, R.; Sarkar, A.; Kruk, R.; Eggert, B.; Brand, R. A.; Wende, H.; Hahn, H. High-Entropy Oxides: An Emerging Prospect for Magnetic Rare-Earth Transition Metal Perovskites. *Phys. Rev. Mater.* **2019**, *3*, 034406.

(5) Sarkar, A.; Kruk, R.; Hahn, H. Magnetic Properties of High Entropy Oxides. *Dat. Trans.* **2021**, *50*, 1973−1982.

(6) Min, L.; Sretenovic, M.; Heitmann, T. W.; Valentine, T. W.; Zu, R.; Gopalan, V.; Rost, C. M.; Ke, X.; Mao, Z. A Topological Kagome Magnet in High Entropy Form. *Commun. Phys.* **2022**, *5*, 63.

(7) Witte, R.; Sarkar, A.; Velasco, L.; Kruk, R.; Brand, R. A.; Eggert, B.; Ollefs, K.; Weschke, E.; Wende, H.; Hahn, H. Magnetic Properties of Rare-Earth and Transition Metal Based Perovskite Type High Entropy Oxides. *J. Appl. Phys.* **2020**, *127*, 185109.

(8) Wu, D.; Kusada, K.; Nanba, Y.; Koyama, M.; Yamamoto, T.; Toriyama, T.; Matsumura, S.; Seo, O.; Gueye, I.; Kim, J.; Rosantha Kumara, L. S.; Sakata, O.; Kawaguchi, S.; Kubota, Y.; Kitagawa, H. Noble-Metal High-Entropy-Alloy Nanoparticles: Atomic-Level Insight into the Electronic Structure. *J. Am. Chem. Soc.* **2022**, *144*, 3365−3369.

(9) Sarkar, A.; Eggert, B.; Velasco, L.; Mu, X.; Lill, J.; Ollefs, K.; Bhattacharya, S. S.; Wende, H.; Kruk, R.; Brand, R. A.; Hahn, H. Role of Intermediate 4*f* States in Tuning the Band Structure of High Entropy Oxides. *APL Mater.* **2020**, *8*, 051111.

(10) Katzbaer, R. R.; dos Santos Vieira, F. M.; Dabo, I.; Mao, Z.; Schaak, R. Band Gap Narrowing in a High-Entropy Spinel Oxide Semiconductor for Enhanced Oxygen Evolution Catalysis. *J. Am. Chem. Soc.* **2023**, *145*, 6753−6761.

(11) Yang, Y.; Peltier, C. R.; Zeng, R.; Schimmenti, R.; Li, Q.; Huang, X.; Yan, Z.; Potsi, G.; Selhorst, R.; Lu, X.; Xu, W.; Tader, M.; Soudackov, A.; Zhang, H.; Krumov, M.; Murray, E.; Xu, P.; Hitt, J.; Xu, L.; Ko, H. Y.; Ernst, B. G.; Bundschu, C.; Luo, A.; Markovich, D.; Hu, M.; He, C.; Wang, H.; Fang, J.; DiStasio, R. A.; Kourkoutis, L. F.; Singer, A.; Noonan, K. J. T.; Xiao, L.; Zhuang, L.; et al. Electrocatalysis in Alkaline Media and Alkaline Membrane-Based Energy Technologies. *Chem. Rev.* **2022**, *122*, 6117−6321.

(12) Zhang, Y.; Lu, T.; Ye, Y.; Dai, W.; Zhu, Y.; Pan, Y. Stabilizing Oxygen Vacancy in Entropy-Engineered $CoFe_2O_4$-Type Catalysts for Co-Prosperity of Efficiency and Stability in an Oxygen Evolution Reaction. *ACS Appl. Mater. Interfaces* **2020**, *12*, 32548−32555.

(13) Jin, Z.; Lyu, J.; Zhao, Y. L.; Li, H.; Lin, X.; Xie, G.; Liu, X.; Kai, J. J.; Qiu, H. J. Rugged High-Entropy Alloy Nanowires with in Situ Formed Surface Spinel Oxide As Highly Stable Electrocatalyst in Zn-Air Batteries. *ACS Mater. Lett.* **2020**, *2*, 1698−1706.

(14) Su, H. Y.; Gorlin, Y.; Man, I. C.; Calle-Vallejo, F.; Norskov, J. K.; Jaramillo, T. F.; Rossmeisl, J. Identifying Active Surface Phases for Metal Oxide Electrocatalysts: A Study of Manganese Oxide Bi-Functional Catalysts for Oxygen Reduction and Water Oxidation Catalysis. *Phys. Chem. Chem. Phys.* **2012**, *14*, 14010−14022.

(15) Gunasooriya, G. T. K. K.; Nørskov, J. K. Analysis of Acid-Stable and Active Oxides for the Oxygen Evolution Reaction. *ACS Energy Lett.* **2020**, *5*, 3778−3787.

(16) McCarroll, W. H.; Katz, L.; Ward, R. Some Ternary Oxides of Tetravalent Molybdenum. *J. Am. Chem. Soc.* **1957**, *79*, 5410−5414.

(17) Brower, W. S.; Fang, P. H. Dielectric Constants of Zinc Tungstate. *J. Appl. Phys.* **1970**, *41*, 2266.

(18) von Weitzel, H. Magnetische Struktur von $CoWO_4$, $NiWO_4$ und $CuWO_4$. *Solid State Commun.* **1970**, *8*, 2071−2072.

(19) Stüßer, N.; Ding, Y.; Hofmann, M.; Reehuis, M.; Ouladdiaf, B.; Ehlers, G.; Günther, D.; Meißner, M.; Steiner, M. Evidence for Interpenetrating Magnetic Structures across an IC-C Phase Transition in $Mn_{0.88}Fe_{0.12}WO_4$. *J. Phys.: Condens. Matter* **2001**, *13*, 2753−2766.

(20) Dachs, H.; Weitzel, H.; Stoll, E. Magnetic Structure of Manganesetungstate $MnWO_4$ at 4.2°K. *Solid State Commun.* **1966**, *4*, 473−474.

(21) Young, A. P.; Schwartz, C. M. High-Pressure Synthesis of Molybdates with the Wolframite Structure. *Science* **1963**, *141*, 348−349.

(22) Reichelt, W.; Weber, T.; Söhnel, T.; Däbritz, S. Mischkristallbildung Im System $CuMoO_4/ZnMoO_4$. *Z. fur Anorg. Allg. Chem.* **2000**, *626*, 2020−2027.

(23) Sleight, A. W.; Chamberland, B. L.; Weiher, J. F. Magnetic, Moessbauer, and Structural Studies on Three Modifications of $FeMoO_4$. *Inorg. Chem.* **1968**, *7*, 1093−1098.

(24) Ito, T.; Takagi, H.; Asano, T. Drastic and Sharp Change in Color, Shape, and Magnetism in Transition of $CuMoO_4$ Single Crystals. *Chem. Mater.* **2009**, *21*, 3376−3379.

(25) Wiesmann, M.; Ehrenberg, H.; Miehe, G.; Peun, T.; Weitzel, H.; Fuess, H. P-T Phase Diagram of $CuMoO_4$. *J. Solid State Chem.* **1997**, *132*, 88−97.

(26) Rodriguez, J. A.; Chaturvedi, S.; Hanson, J. C.; Albornoz, A.; Brito, J. L. Electronic Properties and Phase Transformations in $CoMoO_4$ and $NiMoO_4$: XANES and Time-Resolved Synchrotron XRD Studies. *J. Phys. Chem. B* **1998**, *102*, 1347−1355.

(27) Biesinger, M. C.; Payne, B. P.; Grosvenor, A. P.; Lau, L. W. M.; Gerson, A. R.; Smart, R. S. C. Resolving Surface Chemical States in XPS Analysis of First Row Transition Metals, Oxides and Hydroxides: Cr, Mn, Fe, Co and Ni. *Appl. Surf. Sci.* **2011**, *257*, 2717−2730.

(28) Biesinger, M. C.; Lau, L. W. M.; Gerson, A. R.; Smart, R. S. C. Resolving Surface Chemical States in XPS Analysis of First Row Transition Metals, Oxides and Hydroxides: Sc, Ti, V, Cu and Zn. *Appl. Surf. Sci.* **2010**, *257*, 887−898.

(29) Naumkin, A. V.; Kraut-Vass, A.; Gaarenstroom, S. W.; Powell, C. J. *NIST X-ray Photoelectron Spectroscopy Database*. Version 4.1. (accessed 2023).

(30) Tiwari, A.; Singh, V.; Nagaiah, T. C. Tuning the $MnWO_4$ Morphology and its Electrocatalytic Activity towards Oxygen Reduction Reaction. *J. Mater. Chem. A* **2018**, *6*, 2681−2692.

(31) Baltrusaitis, J.; Mendoza-Sanchez, B.; Fernandez, V.; Veenstra, R.; Dukstiene, N.; Roberts, A.; Fairley, N. Generalized Molybdenum Oxide Surface Chemical State XPS Determination via Informed Amorphous Sample Model. *Appl. Surf. Sci.* **2015**, *326*, 151−161.

(32) *X-ray Photoelectron Spectroscopy (XPS) Reference Pages* https://www.xpsfitting.com (accessed Feb 13, 2023)

(33) McAlister, S. P.; Strobel, P. Magnetic Order in $M_2Mo_3O_8$ Single Crystals (M = Mn, Fe, Co, Ni). *J. Magn. Magn. Mater.* **1983**, *30*, 340−348.

(34) Morey, J. R.; Scheie, A.; Sheckelton, J. P.; Brown, C. M.; McQueen, T. M. $Ni_2Mo_3O_8$: Complex Antiferromagnetic Order on a Honeycomb Lattice. *Phys. Rev. Mater.* **2019**, *3*, 014410.

(35) Mo, S.; Katayama, T.; Chikamatsu, A.; Kitamura, M.; Horiba, K.; Kumigashira, H.; Hasegawa, T. Epitaxial-Strain-Induced Spontaneous Magnetization in Polar $Mn_2Mo_3O_8$. *Chem. Mater.* **2021**, *33*, 7713−7718.

(36) Sethi, Y. A.; Kulkarni, A. K.; Ambalkar, A. A.; Khore, S. K.; Gunjal, A. R.; Gosavi, S. W.; Kale, B. B. CdS Decorated $MnWO_4$ Nanorod Nanoheterostructures: A New 0D-1D Hybrid System for Enhanced Photocatalytic Hydrogen Production under Natural Sunlight. *Nanoscale Adv.* **2021**, *3*, 508−516.

(37) Liu, C.; Lü, H.; Yu, C.; Wu, X.; Wang, P. Hydrothermal-Assisted Microemulsion Synthesis of $FeWO_4$ Nanorods and Their Superior Visible-Light- Driven Photocatalytic Activity. *Mater. Lett.* **2019**, *257*, 126707.

(38) Zhang, H.; Tian, W.; Li, Y.; Sun, H.; Tadé, M. O.; Wang, S. Heterostructured WO_3@$CoWO_4$ Bilayer Nanosheets for Enhanced Visible-Light Photo, Electro and Photoelectro-Chemical Oxidation of Water. *J. Mater. Chem. A* **2018**, *6*, 6265−6272.

(39) Li, M.; Yokoyama, S.; Takahashi, H.; Tohji, K. Bandgap Engineering of $NiWO_4$/CdS Solid Z-Scheme System via an Ion-Exchange Reaction. *Appl. Catal., B* **2019**, *241*, 284−291.

(40) Gaillard, N.; Chang, Y.; Deangelis, A.; Higgins, S.; Braun, A. A Nanocomposite Photoelectrode Made of 2.2 eV Band Gap Copper Tungstate ($CuWO_4$) and Multi-Wall Carbon Nanotubes for Solar-Assisted Water Splitting. *Int. J. Hydrogen Energy* **2013**, *38*, 3166−3176.

(41) Dong, X.; Katzbaer, R. R.; Chitara, B.; Han, L.; Yang, L.; Schaak, R. E.; Yan, F. Optimizing the Synergistic Effect of $CuWO_4$/CuS Hybrid Composites for Photocatalytic Inactivation of Pathogenic Bacteria. *Environ. Sci.: Nano* **2022**, *9*, 4283−4294.

(42) Bi, J.; Wu, L.; Li, Z.; Ding, Z.; Wang, X.; Fu, X. A Facile Microwave Solvothermal Process to Synthesize $ZnWO_4$ Nanoparticles. *J. Alloys Compd.* **2009**, *480*, 684−688.

(43) Sturza, M.; Han, F.; Shoemaker, D. P.; Malliakas, C. D.; Chung, D. Y.; Jin, H.; Freeman, A. J.; Kanatzidis, M. G. $NaBa_2Cu_3S_5$: A Doped p-Type Degenerate Semiconductor. *Inorg. Chem.* **2013**, *52*, 7210−7217.

(44) McCrory, C. C. L.; Jung, S.; Peters, J. C.; Jaramillo, T. F. Benchmarking Heterogeneous Electrocatalysts for the Oxygen Evolution Reaction. *J. Am. Chem. Soc.* **2013**, *135*, 16977−16987.

(45) Asnavandi, M.; Yin, Y.; Li, Y.; Sun, C.; Zhao, C. Promoting Oxygen Evolution Reactions through Introduction of Oxygen Vacancies to Benchmark NiFe-OOH Catalysts. *ACS Energy Lett.* **2018**, *3*, 1515−1520.

(46) Burke, M. S.; Enman, L. J.; Batchellor, A. S.; Zou, S.; Boettcher, S. W. Oxygen Evolution Reaction Electrocatalysis on Transition Metal Oxides and (Oxy)Hydroxides: Activity Trends and Design Principles. *Chem. Mater.* **2015**, *27*, 7549−7558.

(47) Brahlek, M.; Gazda, M.; Keppens, V.; Mazza, A. R.; McCormack, S. J.; Mielewczyk-Gryń, A.; Musico, B.; Page, K.; Rost, C. M.; Sinnott, S. B.; et al. What Is in a Name: Defining "High Entropy" Oxides. *APL Mater.* **2022**, *10*, 110902.

(48) Svane, K. L.; Rossmeisl, J. Theoretical Optimization of Compositions of High-Entropy Oxides for the Oxygen Evolution Reaction. *Angew. Chem., Int. Ed.* **2022**, *61*, No. e202201146.

(49) Mancheva, M. N.; Iordanova, R. S.; Klissurski, D. G.; Tyuliev, G. T.; Kunev, B. N. Direct Mechanochemical Synthesis of Nanocrystalline $NiWO_4$. *J. Phys. Chem. C* **2007**, *111*, 1101−1104.

(50) Nakayama, S.; Nakamura, R.; Akaki, M.; Akahoshi, D.; Kuwahara, H. Ferromagnetic Behavior of $(Fe_{1-y}Zn_y)_2Mo_3O_8$ ($0 \leq y \leq 1$) Induced by Nonmagnetic Zn Substitution. *J. Phys. Soc. Jpn.* **2011**, *80*, 104706.